

Starburst–driven galactic outflows

Biman B. Nath¹ & Joseph Silk²

1. Raman Research Institute, Sadashiva Nagar, Bangalore 560080, India

2. Department of Astrophysics, University of Oxford and Beecroft Institute for Particle Astrophysics and Cosmology Denys Wilkinson Building, Keble Road, OX1 3RH Oxford, UK

8 January 2014

ABSTRACT

We propose a model of starburst–driven galactic outflows whose dynamics depends on both radiation and thermal pressure. Standard models of thermal pressure–driven winds fail to explain some key observations of outflows at low and high redshift galaxies. We discuss a scenario in which radiation pressure from massive stars in a stellar population drive a shell of gas and dust. Subsequent supernova (SN) explosions from the most massive stars in this population then drive stellar ejecta outward in a rarefied medium, making it collide with the radiation pressure driven shell. The collision imparts renewed momentum to the shell, and the resulting re-acceleration makes the shell Rayleigh-Taylor unstable, fragmenting the shell. We show that the speed of these ballistic fragments can explain some recently observed correlations in Lyman break galaxies between wind speed, reddening and star formation rate.

Key words: galaxies:evolution – galaxies:starburst – intergalactic medium

1 INTRODUCTION

Removal of gas from galaxies in the form of outflows constitute an important phase in the evolution of galaxies, and an important mechanism of feedback from galaxies to the surrounding medium. At low redshift, outflows have been directly observed in many galaxies, in optical to X-rays, and at high redshifts, spectroscopic studies have found many examples of outflows. Outflows have been ascribed to either the stellar population in a galaxy or active galactic nuclei, or both (see Veilleux, Cecil, & Bland-Hawthorn 2005, for a recent review).

In the standard scenario of starburst–driven galactic outflows, thermal pressure builds up in the interstellar medium (ISM) of a galaxy owing to supernovae shocks that results from formation of stars, and the pressure of the hot gas then removes a fraction of the ISM in the form of an outflow (Veilleux, Gerald, Bland-Hawthorn 2005, and references therein). The pressure of the hot gas is directly related to the rate of supernovae, or, equivalently to the star formation rate. This scenario, however, has difficulty in explaining some key observations at both low and high redshifts.

Starburst–driven winds observed in nearby galaxies through NaI absorption lines show a correlation between the maximum speed of clouds embedded in the outflow, and the star formation rate (Martin 2005). This can be explained by ram pressure–driven clouds embedded in the outflow, except for very large outflow speeds (Murray, Quataert & Thompson 2005) that may require radiation pressure (Veilleux, Gerald, Bland-Hawthorn 2005). Martin (2005) also showed a

correlation between maximum cloud speed and the rotation speed of host galaxies, which she suggested is an indication of dominant contribution from radiation pressure.

Murray, Quataert & Thompson (2005) have discussed the basic dynamics of a radiatively driven shell of gas and dust. Using these models, Martin (2005) showed that her data was indicative of a feedback mechanism on the star formation process, in which the star formation rate was regulated by gas removal through radiation pressure.

At high redshifts, Shapley et al. (2003) studied a set of ~ 800 Lyman break galaxies (LBG) at $z \sim 3$, and found that the doppler shift speed $\Delta v = v_{em} - v_{ab}$ of the Lyman- α line is correlated with the star formation rate (as implied by the \mathcal{R} luminosity), as well as with the reddening due to dust. The outflow speed (which is related to Δv) was also found to be correlated with the equivalent width of low ionization absorption lines. Taken together with the correlation with the reddening, this suggested that most of the reddening and low ionization absorption occurred in the same region, near the clouds responsible for the doppler shift.

Furthermore, Ferrara and Ricotti (2006) suggested after studying the outflow speed ($V_w \sim 0.5\Delta v$) and the SFR (\dot{M}) that it was difficult to explain the relation with thermal pressure–driven winds. The observed relation is approximately $V_w \propto \dot{M}^{2/3}$. On the contrary, in the standard SN–driven wind via the Sedov-Taylor phase of SN shells, one expects $V_w \propto E^{1/5}$, where $E \propto \dot{M}$ is the rate of energy deposited by the SN.

The correlation between reddening and wind speed observed in LBGs motivates us to seek a model where radiation

pressure is a dominant feature. In the case of a purely radiatively driven shell of gas, the speed is proportional to the star formation rate (Murray et al. 2005), so it is not clear whether one can explain the above mentioned correlations with radiation pressure alone. At the same time, it is reasonable to assume that if the pressure of continuum radiation comes mostly from massive stars (the continuum dust opacity being larger in the blue than in the red), then these stars would also explode earlier than the rest of the stellar population. It is conceivable that a radiatively driven wind shell is pushed by thermal pressure from SN explosions at a later epoch.

Here we study a hybrid model in which first a radiation pressure-driven wind is formed, and a shell moves outward. Then, after a few million years, supernova explosions of the most massive stars will drive their stellar ejecta through a comparatively rarefied medium, and will collide with the radiatively driven shell. The shell will become vulnerable to fragmentation at this stage from Rayleigh-Taylor instability, and the resulting clouds will move ballistically through the ISM, with the momentum acquired from the collision. We show that this model explains the correlation between outflow speed and SFR. In addition, in this model, the dust in the cloud, responsible for the dynamics of the radiatively driven shell, can explain the relation between reddening and outflow speed, as observed in LBGs.

2 WIND DYNAMICS

2.1 Phase 1: radiation pressure-driven wind

We first study a radiatively driven shell of gas and dust. We assume a point source of radiation, of luminosity L , and assume a spherically symmetric shell of gas at distance r . Suppose the total mass (including dark matter) contained within this distance is $M(r)$. Setting κ to be the opacity of matter (dust plus gas) per unit mass of gas (in $\text{cm}^2 \text{gm}^{-1}$), and ignoring gas pressure inside the cavity of the shell, the equation of motion of the gas shell is given by

$$\frac{dV}{dt} = -\frac{GM(r)}{r^2} + \frac{\kappa L}{4\pi r^2 c} - \frac{3V^2}{r}. \quad (1)$$

In a time-independent case, this equation can be rewritten for a wind, and solved for the wind speed at a given radius r , as (ignoring the last term, which refers to deceleration due to swept-up mass; see Murray, Quataert & Thompson 2005),

$$\frac{1}{2}V(r)^2 = \int_{R_0}^r \frac{GM(r)}{r^2} \left(\frac{L}{L_{Ed}(r)} - 1 \right). \quad (2)$$

Here $L_{Ed}(r) = \frac{4\pi GM(r)c}{\kappa}$ is the Eddington luminosity relevant for the given radius r given the mass distribution $M(r)$ and opacity κ . The star formation rate corresponding to $L_{Ed}(r)$ is given by $\dot{M}_* \sim L_{Ed}(r)/(0.007c^2)$. For a singular isothermal mass distribution with velocity dispersion σ ($M(r) = 2\sigma^2 r/G$), this star formation rate is $\sim 50\sigma_{200}^2 (r/10 \text{ kpc}) M_\odot \text{yr}^{-1}$, for $\kappa \sim 500 \text{ cm}^2 \text{gm}^{-1}$ and where $\sigma = 200\sigma_{200} \text{ km s}^{-1}$.

2.2 Dust opacity

Many observations of galactic outflows indicate the presence of dust grains in the outflowing gas. Martin (2005) has noted that the absence of NaI emission indicates absorption by dust, and that cold dust is often found in starburst galaxies at larger scale heights than those of the stars. Opacities of order $\kappa \sim 500 \text{ cm}^2 \text{gm}^{-1}$ can be provided by dust grains through continuum absorption and scattering (Draine & Lee 1984). The absorption opacity of gas mixed with dust is expected to be larger at shorter wavelengths: $\kappa \sim 600\text{--}100 \text{ cm}^2 \text{gm}^{-1}$ at $\lambda \sim 1000\text{--}6000 \text{ \AA}$ (Li & Draine 2001). Observations of reddening of local (Calzetti 2001 and references therein) and high redshift starburst galaxies (Sanders & Mirabel 1996), including LBGs (Adelberger & Steidel 2000) also suggest dust opacities of this order. In our calculations described below, we assume dust opacity of order $\kappa \sim 500 \text{ cm}^2 \text{g}^{-1}$.

2.3 Evolution in luminosity

Consider the case of a single burst of star formation with an initial mass function (IMF) $\phi(m) = \phi_1(m/m_1)^{-(1+x)}$, which is normalized as $M_o = M_o \int m\phi(m)dm$, where M_o is the total mass of the stellar population. The total luminosity of main sequence stars in a stellar population evolves as,

$$L(t) \propto \int_{m_1}^{m_u} \phi(m)l(m)dm \sim \frac{M_o\phi_1 m_1 l_1}{\alpha - x} (t/\tau_1)^{\frac{(\alpha-x)}{(1-\alpha)}}, \quad (3)$$

where $l(m) = l_1(m/m_1)^\alpha$ is the main sequence luminosity of a star with mass m , and $\alpha \sim 3.5$. The main sequence lifetime of a star with mass m_1 is denoted here by τ_1 . Stars on the giant branch contribute more to the luminosity, and their contribution can be incorporated by including a multiplicative factor $[1 + G(t)]$, where $G(t) = \frac{\alpha-x}{\alpha-1} \frac{l_g \tau_g}{l_g(m_{tn})t}$, and l_g, τ_g are the giant branch luminosity and lifetime on the giant branch, and m_{tn} is the turn-off mass at time t (Tinsley 1980). The ratio $G(t)$ is of order unity for short wavelengths (although larger for longer wavelengths, where giant branch stars contribute most), and so we multiply the expression in equation 3 by a factor 2.

In the case of continuous star formation, with a constant SFR, it can be shown that the luminosity evolves as

$$L(t) \approx \frac{[1 + G(t)]\dot{M}\phi_1 m_1 l_1}{\alpha - x} (t/\tau_1)^{\frac{1-\alpha}{1-x}} \approx 4 \times 10^9 L_\odot \dot{M}_1 t_6^{0.14}, \quad (4)$$

where $t_6 = t/1 \text{ Myr}$, $\dot{M}_1 = \dot{M}/1 M_\odot \text{yr}^{-1}$, and where we have assumed a Salpeter IMF ($x = 1.35$), and that $G(t) \sim 1$. We use this expression for luminosity in equation 1 for our calculations below.

2.4 Phase 2: supernova explosions

Next, we consider the evolution of the stellar ejecta from supernova explosions of the most massive stars in this population. The ejecta will move through a rarefied medium in the interior of the radiatively driven shell, since a large fraction of gas is expected to be swept out earlier by radiation pressure. We consider supernovae resulting from the early stages of a starburst, within an interval $t_{sn} \sim 3 \text{ Myr}$, which is the main sequence lifetime of stars with $M > 15M_\odot$. Assuming a Salpeter IMF, one gets a total mass of ejecta

(ignoring the remnant masses), as $M_{ej} \sim 0.1\dot{M}t_{sn}$, considering supernovae for $M > 15M_{\odot}$, and a lower and upper mass cut-offs of 0.1 and $125M_{\odot}$. The total energy output is related to the number of SN, $\sim 0.003\dot{M}t_{sn}$, again assuming a Salpeter IMF and supernovae for $M > 15M_{\odot}$. We assume an energy output of 10^{51} ergs per supernova, so that the total energy output is $E_{ej} = 10^{51}\text{erg} \times 0.003\dot{M}t_{sn}$.

We also assume that the evacuated and rarefied ISM in the interior of the radiatively driven shell has a particle density $n = n_r$. In the Sedov-Taylor phase (which is valid since the ejecta travel with high speed until colliding with the radiatively driven shell, and since the shell does not sweep up much matter in the rarefied medium to slow it down), we have for the evolution of the outer shell of the ejecta (e.g., Shull & Silk 1979),

$$\begin{aligned} R_{ej} &\approx 9.89 \times 10^{-2} \text{ kpc } E_{ej,51}^{0.2} n_{r,1}^{-0.2} t_6^{0.4} \\ V_{ej} &\approx 38.69 \text{ kms}^{-1} E_{ej,51}^{0.2} n_{r,1}^{-0.2} t_6^{-0.6}, \end{aligned} \quad (5)$$

where $E_{ej,51} = E_{ej}/10^{51}$ erg, and $n_{r,1} = n_r/1 \text{ cm}^{-3}$.

2.5 Re-acceleration of the shell and growth of instability

The radiatively driven shell is first accelerated for a short period, and then soon begins to decelerate as the shell radius r increases and the radiation pressure (which scales as r^{-2}) falls. At the same time, the shell of ejecta from subsequent SN events moves swiftly through the rarefied medium inside the radiatively driven shell, and catches up with it at a time t_{coll} , when they collide. The speed of the ejecta is in general much larger than the shell speed, and although the ejecta mass is very small, the momentum imparted to the shell by the colliding ejecta is large. Therefore, the shell is carried forward by the increased momentum from the ejecta coming up behind it. The resulting speed of the shell is given by

$$v = (M_{ej}V_{sn} + M_{shell}V_{shell})/(M_{ej} + M_{shell}), \quad (6)$$

where M_{shell} and V_{shell} are the swept-up mass in the shell and the speed of the shell at the time of collision, and V_{sn} is the speed of the ejecta at that time.

After the collision, the wind shell is re-accelerated, and we have the case of a heavy fluid (in the shell) above a rarefied medium, both being acted upon by an effective gravity resulting from the acceleration of the shell. The shell material is therefore subject to Rayleigh-Taylor (RT) instabilities, and is liable to fragmentation.

Even before the collision, the expanding shell is prone to dynamical and gravitational instabilities. Vishniac (1983) estimated the shortest growth time for gravitational instability to be given by $t_g \sim c_s/\pi G\sigma$, where σ is the surface mass density. A lower limit on the growth time for instability is obtained by assuming a cool shell with $T \sim 10^4$ K.

After the collision, the shell is re-accelerated, and becomes Rayleigh-Taylor unstable. The effective gravitational acceleration at this time is $g_{eff} \sim v^2/r$. The time scale of Rayleigh-Taylor instability for clouds of size $\lambda = 2\pi/k$ is given by,

$$\tau_{RT} \sim (g_{eff}k)^{-1/2} \sim (\lambda/2\pi g_{eff})^{1/2}, \quad (7)$$

where k is the wavenumber.

3 RESULTS

We follow the evolution of the radiatively driven shell (eqn 1) numerically and track the trajectory of SN ejecta (eqn 5), and determine the time of collision (t_{coll}) between the two. For the dark matter profile, we have assumed the galaxies to be of total mass $M = 10^{12}M_{\odot}$, at $z = 3$, and assumed a Navarro-Frenk-White halo profile, with a concentration parameter $c = 3$ (Navarro, Frenk, White 1996). Our assumption is motivated by the estimate made by Adelberger et al. (2005) from the clustering of LBGs and comparison with N-body simulations. The median halo mass of LBGs at $z \sim 3$ is estimated to be $10^{11.86 \pm 0.3} M_{\odot}$. Although there is considerable uncertainty in the dynamical mass estimate of LBGs (see Weatherley & Warren 2005), our results are not sensitive to the gravitational deceleration of the shell by dark matter, and therefore, to the assumption of total mass and its profile.

Figure 1 shows the evolution of the shell radius (solid line, top panel) and speed (solid line, bottom panel) with time, for a star formation rate of $\dot{M} = 100 M_{\odot} \text{ yr}^{-1}$, a continuum dust opacity $\kappa = 500 \text{ cm}^2 \text{ gm}^{-1}$. The particle density in the undisturbed ISM (that the radiatively driven shell sweeps through) is assumed to be $n_g = 5 \text{ cm}^{-3}$, and the density inside the shell is assumed to be $n_r = 0.01 \text{ cm}^{-3}$. It is seen that the shell accelerates for an initial brief period ($\ll 1$ Myr), after which it continuously decelerates, mostly owing to the decrease in radiation pressure with distance, and to some extent, to the growing weight of the swept-up mass in the shell.

The dotted lines in Figure 1 show the corresponding evolution for the stellar ejecta, which we assumed to expand outward after a period of $t_{sn} \sim 3$ Myr. The rarefied medium inside the radiatively driven shell helps the ejecta move with high speed, and catch up with the shell within a short time.

Figure 2 plots the (logarithm of the) ratio of the shortest time-scale for instability to the age of the shell, as a function of time. The dotted line shows the shortest time-scale for gravitational instability, assuming a cool shell with gas at $T \sim 10^4$ K. The surface mass density is calculated from the swept-up mass within r , the shell radius. The figure shows that gravitationally unstable modes takes $\gg 10$ Myr to grow, although the time-scale for growth steadily decreases with time, due to the increasing surface mass density.

After the collision, the shortest time-scale for RT instability is calculated by using equation 7 for instabilities of wavelength $\sim 2\pi r$, where r is the shell radius. This is the largest wavelength for instabilities in the shell, and therefore gives the time-scale for the fastest growing mode. This time-scale at the time of collision is shown as a point. The effective gravitational acceleration at this time is $g_{eff} \sim v^2/r \sim 10^{-7} \text{ cm s}^{-2}$, for $\dot{M} \sim 100 M_{\odot} \text{ yr}^{-1}$, making the shortest time-scale for instability growth comparable to the age of the shell (a few Myr). The re-acceleration of the shell, therefore, makes it prone to RT instabilities. This is likely to feed gravitational instabilities on scales that are gravitationally stable at this stage.

The size of the resulting fragments will be 1–1.5 kpc, the shell radius at this point of time, as plotted in Figure 3 as a function of the outflow speed for the assumed values of the parameters. We then identify the speed of the

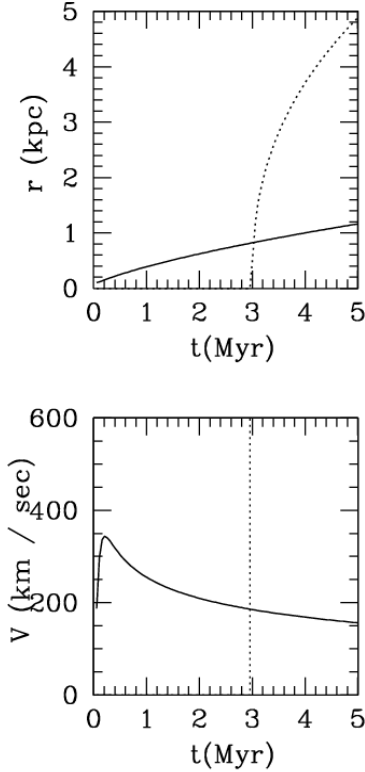


Figure 1. The top panel plots the shell radius (kpc) with time (Myr) (solid line), for a star formation rate of $100 M_{\odot}$ per year, with ambient gas density $n_g = 5$ per cc, and for opacity $\kappa = 500 \text{ cm}^2 \text{ gm}^{-1}$. The dotted line shows the evolution of the hot gas bubble, assuming a density inside the shell $n_r = 0.01$ per cc. The bottom panel shows the corresponding speed of the shell (solid line) and the hot bubble (dotted line).

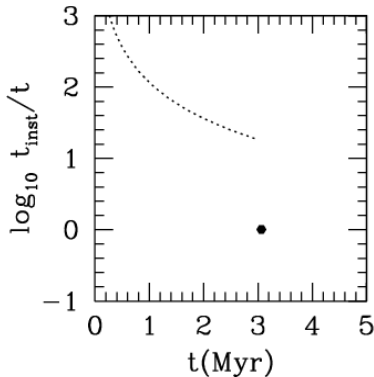


Figure 2. The ratio between the instability growth time-scale and age of the shell (in logarithmic units) is plotted with time. The dotted line shows the shortest time-scale for gravitational instability, assuming a shell temperature of 10^4 K. For most of the time span, the shell decelerates and so there is no RT instability, but after the collision, it is accelerated, and the ratio of RT timescale and age of the shell is shown as a point at the time of collision.

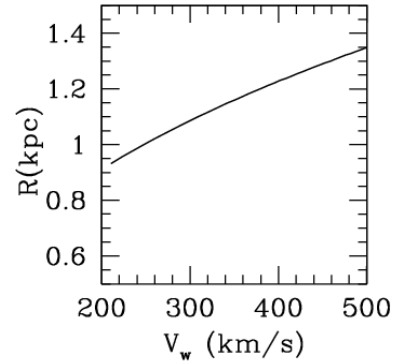


Figure 3. The shell radius at t_{coll} as a function of outflow speed (in km/s) for the same set of parameters as in Figure 1.

cloud after collision as the outflow speed, V_w . We can then compare our results with data from Shapley et al. (2003), for different assumptions of parameter values. The results of the present model are insensitive to the launching radius and initial speed of the shell, and depends on the assumed values of dust opacity (κ), the densities of gas outside (n_g) and inside (n_r) the shell. We found that the best case scenario needs $\kappa = 500 \text{ cm}^2 \text{ gm}^{-1}$, $n_g = 5 \text{ cm}^{-3}$, and $n_r = 0.01 \text{ cm}^{-3}$.

The top panel of Figure 4 plots the resulting outflow speed with SFR for these parameter values, where we show the result of our calculation with a solid curve, along with data points from Shapley et al. (2003) (their Table 3, with $h = 0.7$). The dashed line in the top panel shows the slope of the expected relation between outflow speed and SFR (scaled arbitrarily) in the case of a shell driven by hot gas ($V_w \propto E^{1/5}$).

Another natural prediction of this scenario is a correlation between outflow speed and reddening due to dust absorption. The outflow speed is determined by the combined momentum of the radiative shell and the ejecta, which is related to the total mass in the shell, and therefore, to the amount of dust in the shell. We can quantify this correlation by estimating the amount of reddening using the column density of material in the shell. The bottom panel of Figure 4 shows the expected reddening ($E(B-V)$) as a function of the cloud speed for three different choices of the reddening versus column density relation. The solid line at the bottom of the figure uses the relation between hydrogen column density and reddening as found in the Small Magellanic Cloud (SMC) ($N_H/E(B-V) = 4.4 \pm 0.7 \times 10^{22} \text{ cm}^2 \text{ mag}^{-1}$; Bouchet et al 1985), with the dotted lines showing the $1 - \sigma$ spread. The short-dashed line uses the calibration from observations of the Large Magellanic Cloud (LMC; $N_H/E(B-V) = 2 \pm 0.5 \times 10^{22} \text{ cm}^2 \text{ mag}^{-1}$; Koornneef et al 1982), and the long-dashed line uses the Galactic ISM data ($N_H/E(B-V) = 4.93 \pm 0.28 \times 10^{21} \text{ cm}^2 \text{ mag}^{-1}$; Diplas & Savage 1994).

4 DISCUSSION

The top panel of Figure 4 shows that the scenario described here, along with suitable assumptions of the values of key parameters ($\kappa = 500 \text{ cm}^2 \text{ gm}^{-1}$, $n_g = 5 \text{ cm}^{-3}$, and $n_r = 0.01$

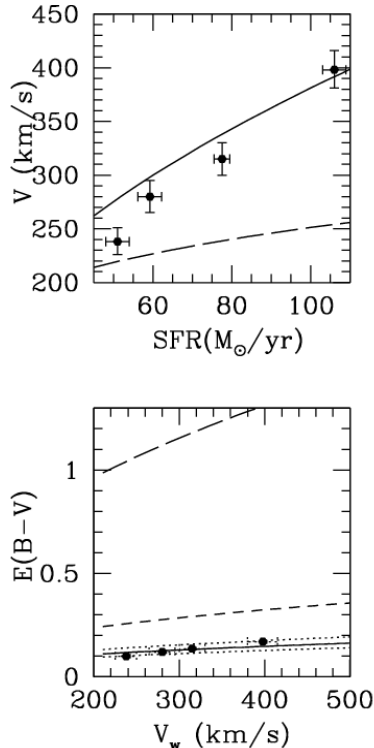


Figure 4. The top panel plots the outflow speed with SFR with a solid curve. The dashed curve is the expected result from a thermal pressure-driven wind. The bottom panel plots the reddening with outflow speed using calibration of column density and $E(B-V)$ from SMC (solid line), LMC (short-dashed line) and Galactic ISM (long-dashed line). The dotted lines show the $1-\sigma$ error margin for the calibration for SMC type dust.

cm^{-3}), can explain the observations of outflows speed and SFR observed in LBGs.

While the calibration of column density and reddening from SMC data explains the data of reddening and outflow speed in LBGs from Shapley et al. (2003), the expected reddening from Galactic ISM calibration is much larger. It should be kept in mind that dust grains are destroyed in ISM shocks by a variety of processes, from energetic grain-grain collisions and from collisions between gas ions and dust grains. Calculations show that large grains (with sizes larger than $\sim 0.05 \mu$) are destroyed in shocks with speed larger than $\sim 200 \text{ km/s}$ (Jones et al. 1997). In the present case, dust grains embedded in the radiatively driven shell coast with a speed $\sim 200 \text{ km s}^{-1}$ for a few Myr before being hit by stellar ejecta (see bottom panel of Figure 1). Afterwards, the fragmented clouds traverse the rest of the ISM at high speed ($v \sim 300\text{--}400 \text{ km s}^{-1}$) and leave the host galaxy within a few Myr, because the typical half-light radius of LBGs is of order $\sim 1 \text{ kpc}$ (see below), comparable to the distance where clouds form in the present scenario. Dust grains in the cloud will therefore be destroyed to a certain extent, especially the larger grains, and the dashed and dotted lines in Figure 4 (bottom panel), corresponding to Galactic and LMC-type dust, will come closer to the LBG data.

Another interesting possibility is that due to the destruction of large grains, the grain size distribution in these clouds will be dominated by smaller ($\leq 500 \text{ \AA}$) grains, and so

the total surface area of grains will increase, thereby increasing the reddening for shorter wavelength ultraviolet continuum. The SMC-type extinction curve shows more reddening at wavelengths shorter than the 2175 \AA feature than the Milky Way extinction curve (e.g., Pei 1992), and so the solid line in Figure 4, corresponding to SMC-type dust, is likely to show increased reddening for larger outflow speeds, thereby bringing the predicted curve closer to the data points in Shapley et al. (2003). At the same time, the smaller grain size would show less reddening in the optical. Therefore, the frequency dependence in reddening for outflows in LBGs will likely change with redshift, as the rest frame wavelength for observed optical radiation changes with redshift.

An important caveat arises from the fact that in comparing with the data, we have identified the outflow speed with $\Delta V/2$, where $\Delta V = |V_{em} - V_{abs}|$. Adelberger et al. (2005) have shown that there are asymmetries between $V_{em} - V_{neb}$ and $V_{abs} - V_{neb}$, where V_{neb} is the speed of the ISM, indicating that outflow speed can significantly differ from $\Delta V/2$, which we have assumed for simplicity.

The scenario discussed here has several implications. Firstly, the shell fragments are generated at radii $\sim 11.5 \text{ kpc}$ (Figure 3), comparable to the half-light radii of LBGs. Bouwens et al. (2004) estimated the mean half-light size of LBGs at $z \sim 3$ as $\sim 1.3 \text{ kpc}$. Therefore, the fragments are likely to penetrate the rest of the galactic ISM and deposit metals into the intergalactic medium (IGM), instead of falling back on to the host galaxies. Galactic outflows have been invoked to explain the metallicity of low column density Lyman- α absorbers in the IGM, and several authors have expressed concern that this process of metal enrichment through outflows might (1) increase the number of absorption lines more than necessary for consistency with models of structure formation, and (2) dynamically disturb the absorption systems. It has been suggested that these problems could be overcome if the wind shell fragments, so that the fragments can coast to large distances (e.g., Theuns, Mo & Schaye 2001). (Recent detailed numerical studies, however, find that galactic winds may not pose a problem for the interpretation of Lyman- α absorption systems as was previously thought (Cen et al. 2005).) We note that galactic wind-driven shells in the scenario discussed here undergo fragmentation even while traversing the ISM, and the fragmented shell is likely to spread metals in the IGM in an inhomogeneous manner, and not dynamically disturb the gaseous filaments responsible for Ly- α absorption systems.

5 ACKNOWLEDGEMENT

We thank the referee for valuable comments.

REFERENCES

- Adelberger, K. L., & Steidel, C. C. 2000, *ApJ*, 544, 218
- Adelberger, K. L., Shapley, A. E., Steidel, C. C., Pettini, M. Erb, D. K. & Reddey, N. A. 2005, *ApJ*, 629, 636
- Adelberger, K. L., Steidel, C. C., Pettini, M., Shapley, A. E., Reddey, N. A. & Erb, D. K. 2005, *ApJ*, 629, 636
- Bouwens, R. J., Illingworth, G. D., Blakeslee, J. P., Broadhurst, T. J., & Franx, M. 2004, *ApJ*, 611, L1

- Calzetti, D. 2001, PASP, 113, 1449
Calzetti, D., Bohlin, R. C., Kinney, A. L., Storchi-Bergmann, T., & Heckman, T. M. 1995, ApJ, 443, 136
Cen, R., Nagamine, K. & Ostriker, J. P. 2005, ApJ, 635, 86
Diplas, A., Savage, B. D. 1994, ApJS, 93, 211
Draine, B. & Lee, H. M. 1984, ApJ, 285, 89
Ferrara, A. & Ricotti, M. 2006, MNRAS, 373, 571
Jones, A. P., Tielens, A. G. G. M., Hollenbach, D. J., McKee, C. F. 1997, AIPC, 402, 595
Koorneef, J. 1982, A&A, 107, 247
Kozasa, T., Hasegawa, H., & Nomoto, K. 1989, ApJ, 344, 325
Martin, C. L. 2005, ApJ, 621, 227
Murray, N., Quataert, Q. & Thompson, T. A. 2005, ApJ, 618, 569
Navarro, J. F., Frenk, C. S., White, S. D. M. 1996, ApJ, 462, 563
Nozawa, T., Kozasa, T., Umeda, H., Maeda, K., & Nomoto, K. 2003, ApJ, 598, 785
Pei, Y. C. 1992, ApJ, 395, 130
Sanders, D. B., & Mirabel, I. F. 1996, ARA&A, 34, 749
Shapley, A. E., Steidel, C. C., Pettini, M. & Adelberger K. L. 2003, ApJ, 588, 65
Shull, J. M., & Silk, J. 1979, ApJ, 234, 427
Theuns, T., Mo, H. J. & Schaye, J. 2001, MNRAS, 321, 450
Tinsley, B. M. 1980, FCPH, 5, 287
Todini, P., & Ferrara, A. 2001, MNRAS, 325, 726
Weatherley, S. J. & Warren, S. J. 2005, MNRAS, 363, L6